

Characterization of microstructure and properties of Al–Al₃Zr–Al₂O₃ composite

ANUP MANDAL*, KARABI DAS and SIDDHARTHA DAS

Department of Metallurgical & Materials Engineering, Indian Institute of Technology, Kharagpur 721 302, India

MS received 9 August 2015; accepted 22 January 2016

Abstract. Aluminium-based metal matrix composite strengthened by *in situ* Al₂O₃ and Al₃Zr particles were synthesized by powder metallurgy route. Phase analysis by X-ray diffraction and scanning electron microscopy revealed that the reaction between Al and ZrO₂ produced Al₂O₃ and Al₃Zr phases in the sintered composites. The hardness of the composite is a strong function of sintering temperature as well as the volume fraction of reinforcements. The dry sliding wear test results clearly indicated that increasing the volume fraction of zirconia particles in the composite improved the wear resistance. Microcutting, ploughing, delamination and oxidation were the main mechanisms of wear.

Keywords. Metal matrix composite; hardness; wear; scanning electron microscopy.

1. Introduction

Motivation for the development of composite is to combine the properties of its constituents. In metal matrix composite, rigid ceramic or intermetallic particulates are embedded in ductile metal matrix. Thus, metal matrix composite combines both the metallic properties (ductility and toughness) and ceramic properties (high hardness, strength and modulus). It is now well recognized that metal matrix composites have a high potential for advanced structural applications [1]. Aluminium is the most popular matrix for the metal matrix composites. Aluminium alloys are quite attractive due to low density, capability to be strengthened by precipitation, good corrosion resistance, high thermal and electrical conductivity and high damping capacity. However, Al alloys possess poor wear and seizure resistance. To improve the above properties, researchers successfully dispersed various hard and soft reinforcements such as SiC [2], Al₂O₃ [3,4], TiC [5], silicon particle [6], carbon fibre [7], graphite [8], fly ash [9], etc. in aluminium alloys by different processing routes. *Ex-situ* particulate reinforced composites suffer from few general drawbacks such as uneven distribution of the reinforcement and nonwetting of the reinforcement and matrix due to surface contamination of the reinforcements. To overcome these limitations, *in-situ* composite where reinforcement is generated during processing has gained prominence. The advantages with *in-situ* composites are (a) clean reinforcement–matrix interface resulting in a strong interfacial bonding, (b) *in-situ* reinforcements are thermodynamically stable and (c) the reinforcement particles are fine in size and their distribution in the matrix is more uniform, yielding better mechanical properties.

Wang *et al* [10] prepared (AlCr)₃Ti-based alloy composite by mechanical milling and annealing process. In a previous work, Zhao *et al* [11] tried to produce Al₂O₃ + Al₃Zr reinforced aluminium composite by magnetochemical melt reduction from Al–Zr(CO₃)₂ system. In recent times, Hossain *et al* [12] have studied the mechanical properties and fracture behaviour of Al–ZrO₂ composite prepared by the casting method. But the melting casting route has disadvantages of inhomogeneity in the structure and chances of dendrite formation. These problems can be solved by using powder metallurgy route. Hence, in this work, Al₂O₃ + Al₃Zr + Al composite was prepared by *in-situ* chemical reaction from the Al–ZrO₂ system. The specific objectives of the present investigation are to synthesize *in-situ* Al₃Zr and Al₂O₃-reinforced Al matrix composite by mechanical milling and conventional powder metallurgy technique, to optimize the sintering temperature for the synthesis of Al–Al₃Zr–Al₂O₃ composite and to study the wear behaviour of the composite.

2. Experimental

Different compositions were selected for the synthesis of aluminium based *in-situ* composites and the designations used are listed in table 1. Commercial aluminium powder with mean particle size of 30 μm and purity of 99.9% and monoclinic zirconia powder (11–39 μm) were used for milling. The mass fractions of ZrO₂ particle were 5, 10 and 20%. Mechanical milling was performed in a planetary ball mill (Fritsch Pulversette P6, single vial ball mill) at room temperature and at a rotation speed of 300 rpm using toluene as the process control agent. Both unmilled and milled samples of Al–ZrO₂ nanocomposites were investigated by a Perkin Elmer Pyris Diamond differential thermal analyzer (DTA) in the temperature range of

*Author for correspondence (anupmetal@gmail.com)

Table 1. Material compositions under study.

Designation	Composition	Matrix	Reinforcements
A5Z	Al + 5 wt% ZrO ₂	Al	Al ₃ Zr, Al ₂ O ₃
A10Z	Al + 10 wt% ZrO ₂	Al	Al ₃ Zr, Al ₂ O ₃
A20Z	Al + 20 wt% ZrO ₂	Al	Al ₃ Zr, Al ₂ O ₃

50–1000°C, with a heating rate of 10°C min⁻¹ in argon atmosphere. DTA was used to understand the effect of milling on the reaction temperature between Al and ZrO₂. The ball-milled Al–ZrO₂ composite powders were compacted using a uniaxial cold press at 4, 5 and 7.5 MPa pressure. Sintering was carried out by heating the individual specimens at 700, 750, 800 and 850°C temperatures in a muffle furnace in argon atmosphere. The nanocomposite powders were studied by the X-ray diffraction (XRD) using a high-resolution Bruker D8 Advance machine with CoK α radiation ($\lambda = 1.79 \text{ \AA}$) and the diffracting angle range was 20–100°. The phases formed were identified by insidious comparison of the recorded diffraction peaks with the ICDD database using X-Pert High Score software. The mirror polished sintered samples were pasted on carbon tape on a specimen holder. The scanning electron microscope (SEM) analysis was carried out using JEOL JSM 5800 machine and also finite element SEM (FESEM) (Carl Zeiss Supra 40). Both bulk and particle energy-dispersive spectroscopy (EDS) analyses were carried out using JEOL JSM 5800 machine. The hardness of the present composites was measured using Vickers's hardness tester at a constant load of 5 kg for a period of 10 s. The prepared composites were subjected to the wear test under a dry sliding condition. Pin-on-disc wear testing machine (Ducom: TR201) was used for carrying out these wear tests. The tangential frictional force and wear were monitored with the help of electronic sensors. The tests were conducted on 10 mm diameter, 10 mm long cylindrical specimens against a rotating 220 grit SiC paper pasted on a steel disc. For each type of material, tests were conducted at an applied load range of 4.9–9.8 N keeping the sliding speed fixed at 200 rpm and track diameter of 70 mm. The worn surfaces of the test material were examined under a SEM. Wear debris was also collected and EDS was performed on each wear debris sample. Height loss of the pin was used to calculate the wear volume loss as a function of sliding distance.

3. Results and discussion

3.1 Powder characterization

3.1a Effect of ball milling on morphology and size of powder: Figure 1a shows SEM micrographs of A5Z powders in the unmilled and different hour milling conditions. Initial aluminium particles are rod-shaped and zirconia particles are agglomerated flower-like particles. The average particle size of aluminium and zirconia particles are in the range of 30–45

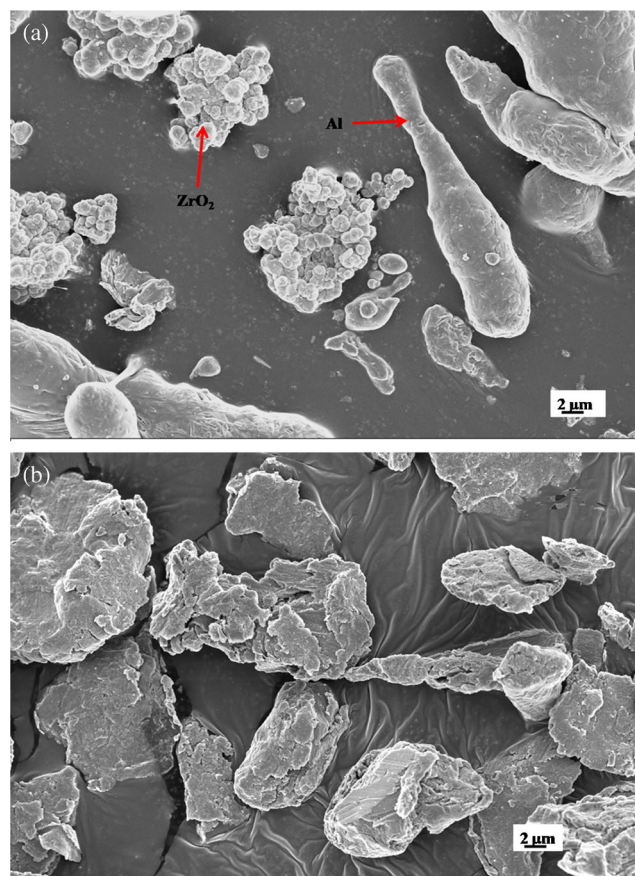


Figure 1. SEM micrographs of milled powders (A5Z): (a) 0 and (b) 15 h.

and 15–30 μm , respectively. The aluminium and zirconia particles cannot be distinguished in figure 1b. High-energy ball milling is a process in which deformation, fracture and re-welding process between powder particles occur continuously and repeatedly. The particle size decreases with the increase in milling time. There is no change in the powder particle size with the increase in milling time, when equilibrium is established between the fractures and welding process [13].

XRD patterns of A5Z composite powders after milling prior to any heat treatment process are shown in figure 2a. Only the peaks of Al and ZrO₂ are present in the XRD pattern. It is observed that there are no phase changes during milling as a function of time. Hence, no reaction occurs between Al and m ZrO₂ during milling up to 15 h. The peak broadening of Al (111) for A5Z powders with increasing milling time is shown in figure 2b. It is observed that all the peaks get broadened with the increase in milling time. This may be due to the reduction in crystallite size and/or increase in induced lattice strain in powder particles. Figure 2c shows the change in crystallite size and lattice strain as a function of milling time for A5Z. The crystallite size and r.m.s lattice strain are calculated from Al (111) peak broadening of XRD powder patterns using X'pert high score software. It is evident that the crystallite size is decreasing rapidly in the first 5 h of milling to approximately 100 nm and

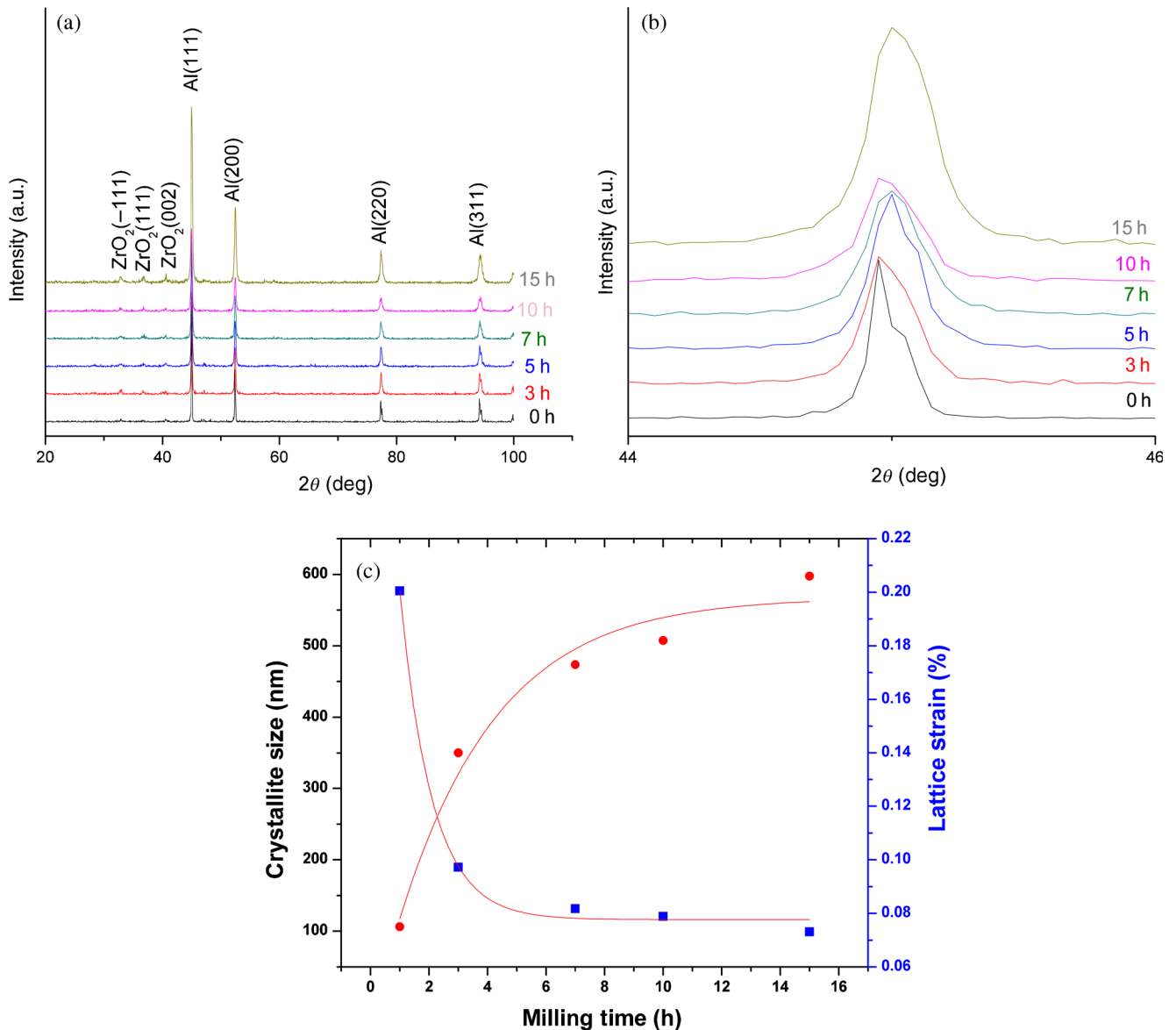


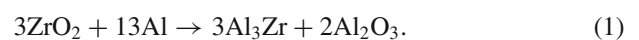
Figure 2. (a) XRD patterns of A5Z powder after different hours of milling, (b) Al (111) peak broadenings for A5Z powder after different hours of milling, (c) variation of crystallite size and r.m.s. lattice strain vs. milling time (A5Z).

after 5 h of milling time, there is no significant change in the crystallite size. The lattice strain increases with the increase in milling time.

3.1b Effect of ball milling on reaction temperature of Al and ZrO₂: Figure 3a shows the DTA curves of the unmilled and 15 h ball-milled A5Z composite powder mixture. Figure 3b shows the DTA curves of the unmilled and 15 h ball-milled A10Z composite mixture powders. It is observed that during heating at the 10°C per min, an endothermic peak develops at ~666°C. This peak arises from heat absorption due to melting of the aluminium component and this is followed by the development of a relatively large exothermic peak at ~1046° and 683°C for unmilled and 15 h milled powders, respectively. Apparently, this peak results from an aluminothermic

reaction between the liquid aluminium and ZrO₂ powders. It is evident from the DTA trace that the reaction temperature for Al–ZrO₂ powder decrease with the increase in milling time. The endothermic peak follows the exothermic peak for unmilled and milled powders; therefore, the exothermic reaction is a liquid–solid reaction.

When the milled powders are subjected to a thermal treatment, there is, in general, a decrease in the reaction onset temperature. The lowering of the onset reaction temperature may be due to (1) an establishment of a good interface contact between the reactants, (2) a refinement of crystallite size and strain to enhance the reactivity of the components, and (3) a decrease in the particle size [13]. The reaction between Al and ZrO₂ particles occurs as follows [14]:



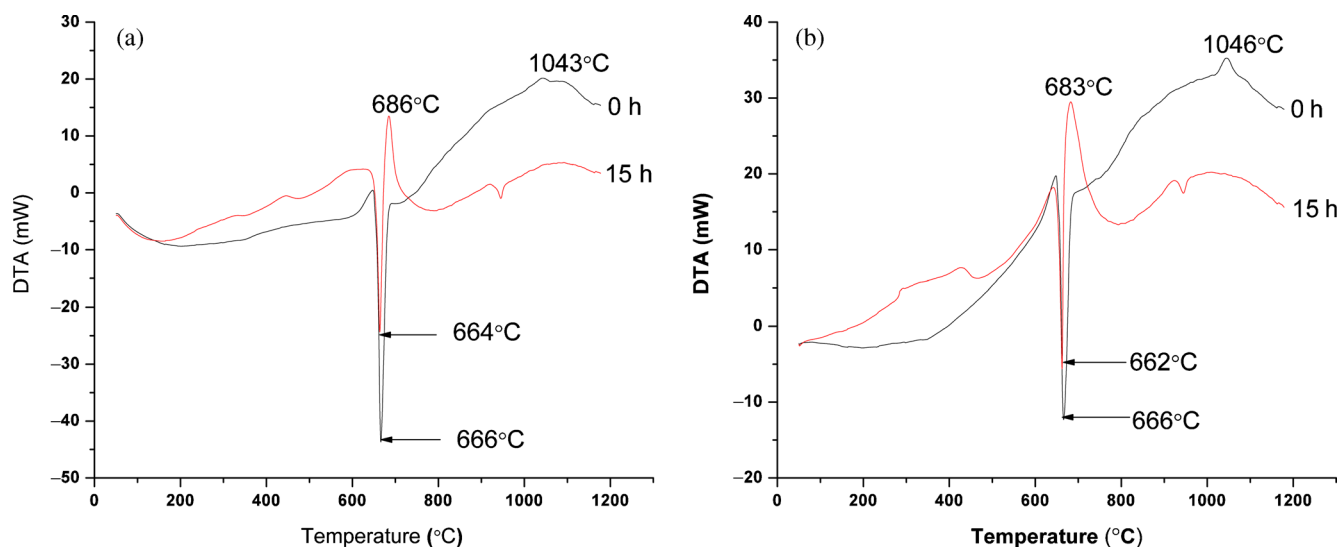


Figure 3. Differential thermal analysis heating traces for milled powders: (a) A5Z and (b) A10Z.

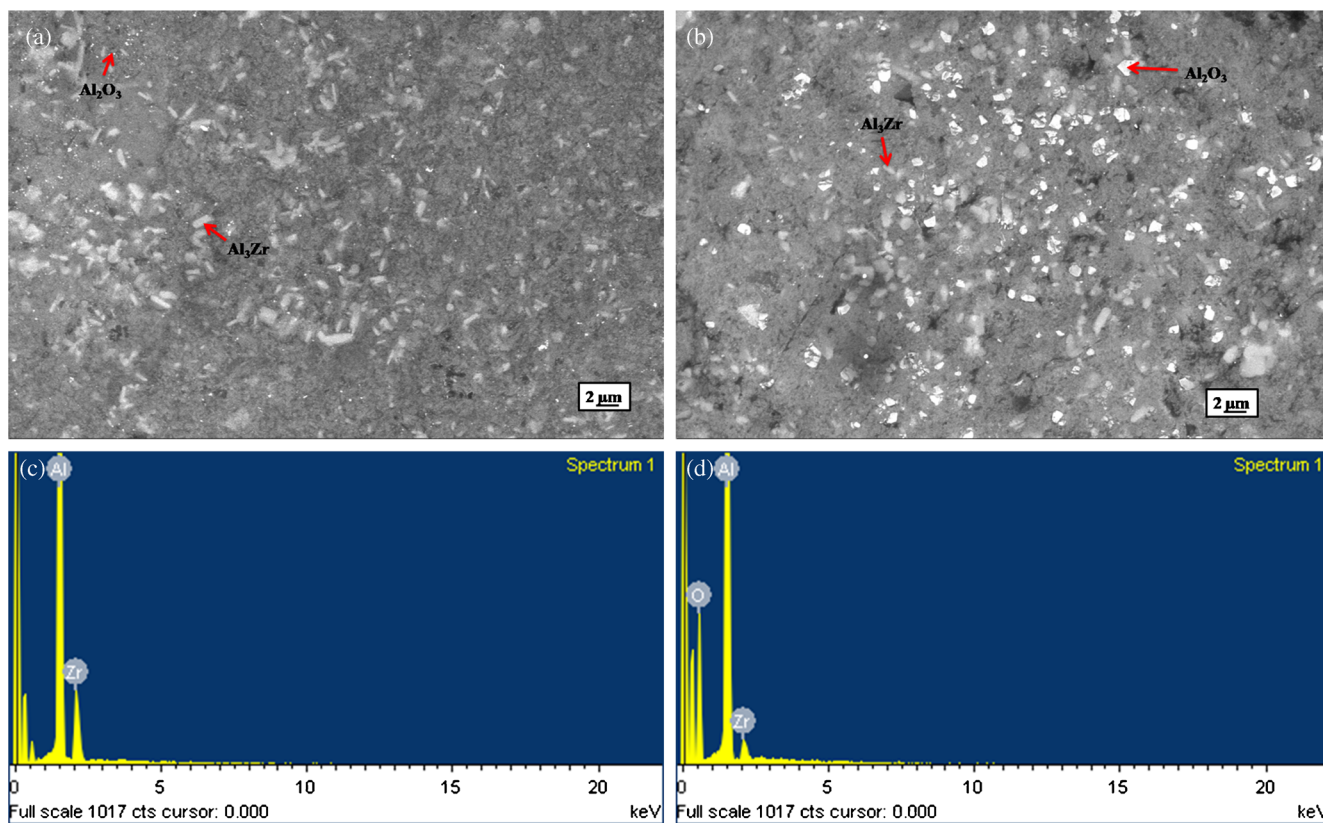


Figure 4. SEM micrographs of A5Z sample sintered at (a) 700 and (b) 750°C. EDS spectrum from (c) Al₃Zr and (d) Al₂O₃.

The thermodynamic parameters are as follows [15]: $\Delta G_{\text{ZrO}_2} = -1082151.4 + 198.52T$; $\Delta G_{\text{Al}} = 5609.9 - 11.35T$; $\Delta G_{\text{Al}_3\text{Zr}} = -25138.3 - 319.4T$; $\Delta G_{\text{Al}_2\text{O}_3} = -1121951.3 + 323.124T$. Gibb's free energy of the reaction is $-106532.3 + 75.79T$ (J mol K⁻¹). As Gibbs free energy is negative, the reaction between Al and ZrO₂ occur spontaneously. The melting points of ZrO₂, Al₃Zr

and Al₂O₃ are 2600, 1350 and 2046°C, respectively, which are all in the solid state in the molten aluminium. It is also evident from figure 3 that higher volume fraction of Zr decreases the reaction temperature. With increasing volume fraction of Zr, more Al reacts with Zr causing high energy release during the reaction. Therefore, the reaction is possible at a lower temperature. Moreover, with increasing

volume fraction of Zr, the surface area and surface energy also increase. Hence, the reaction is favourable at a lower temperature.

3.2 Characterization of sintered samples

3.2a Microstructure: The previous DTA analysis gives an idea of sintering tempering of Al–ZrO₂ composite pallets. Since the reaction temperature is around 683°C, sintering temperature has been selected above this temperature. All

Table 2. EDS analysis results from Al₃Zr particle.

Element	Weight%	Atomic%
Al K	77.85	92.24
Zr L	22.15	7.76
Total	100	100

Table 3. EDS analysis results from Al₂O₃ particle.

Element	Weight%	Atomic%
O K	12.24	19.32
Al K	85.48	80.05
Zr L	2.28	0.63

three composites are sintered at 700, 750, 800 and 850°C. A5Z composite melts and the pellets collapse at 800°C and A10Z composite pellets collapse at 850°C.

Figure 4a and b shows the morphology of sintered compacts of A5Z composite at 700 and 750°C sintering temperatures. Al₃Zr and Al₂O₃ are formed at a sintering temperature of 700°C for A5Z composite. For A5Z composite sintered at 700°C, the elongated particles are Al₃Zr and very small rounded white particles are Al₂O₃ particles. The Al₃Zr particles are uniformly distributed in the aluminium matrix and the size of the Al₂O₃ particles is too small to be visible in SEM. The Al₂O₃ and Al₃Zr particles are identified by EDS spectrum (figure 4c, d). Elemental composition obtained by EDS analysis from Al₃Zr and Al₂O₃ particles are shown in tables 2 and 3, respectively. The average size of Al₃Zr and Al₂O₃ particles are in the range of 1.5–4 and 0.5–1 μm, respectively, for sintering temperature of 700°C. However, with increasing sintering temperature, the Al₂O₃ particles grow in size (1–2 μm) and become clearly visible. A5Z composite deforms due to melting at a sintering temperature of 800°C.

Figure 5a, b and c shows microstructures of sintered compacts of A10Z sintered at 700, 750 and 800°C, respectively. The morphology of A10Z composite is almost the same as A5Z composite. The only difference is that the fractions of Al₃Zr particles are much higher. The Al₂O₃ particles remain

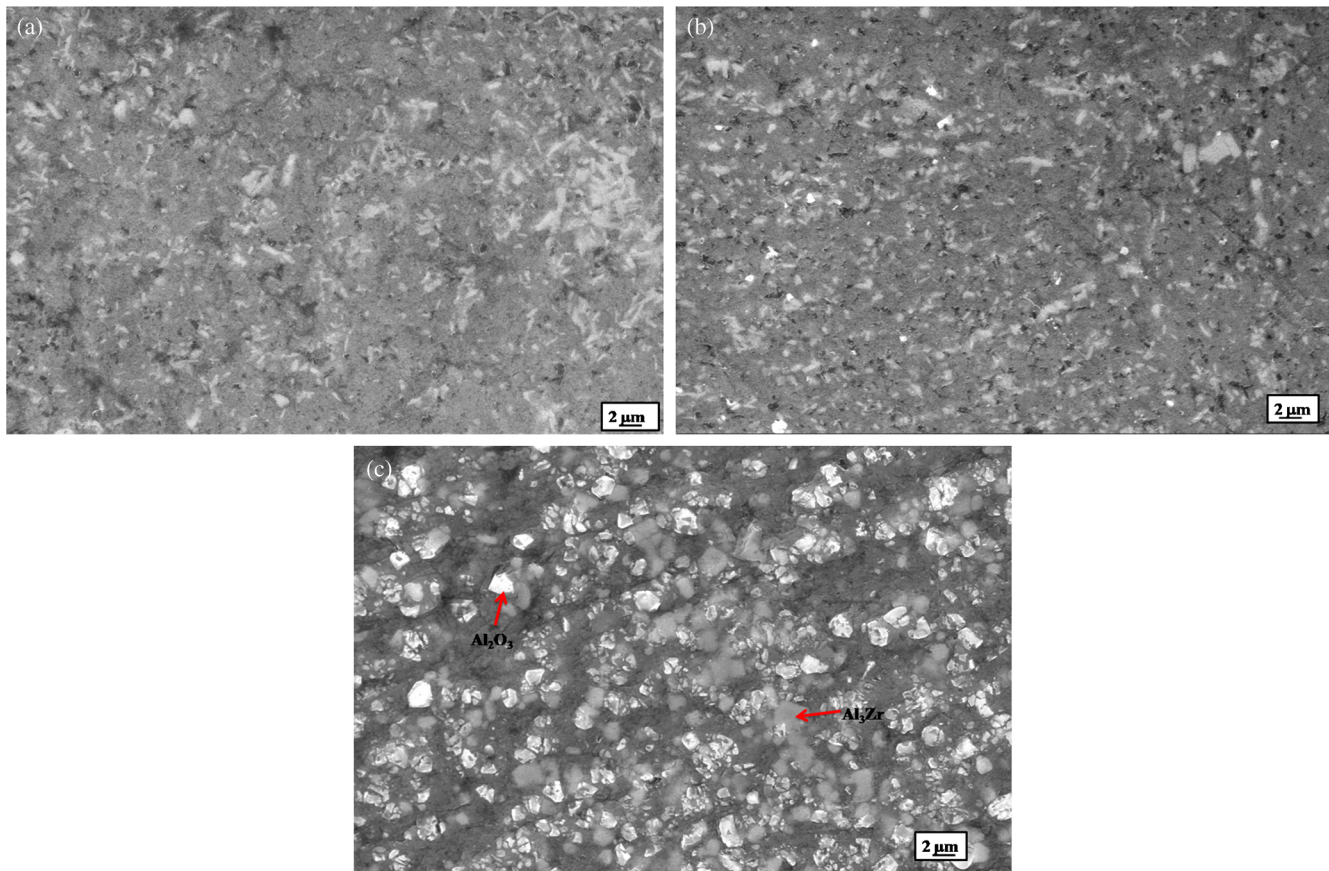


Figure 5. SEM micrographs of A10Z sample sintered at (a) 700, (b) 750 and (c) 800°C.

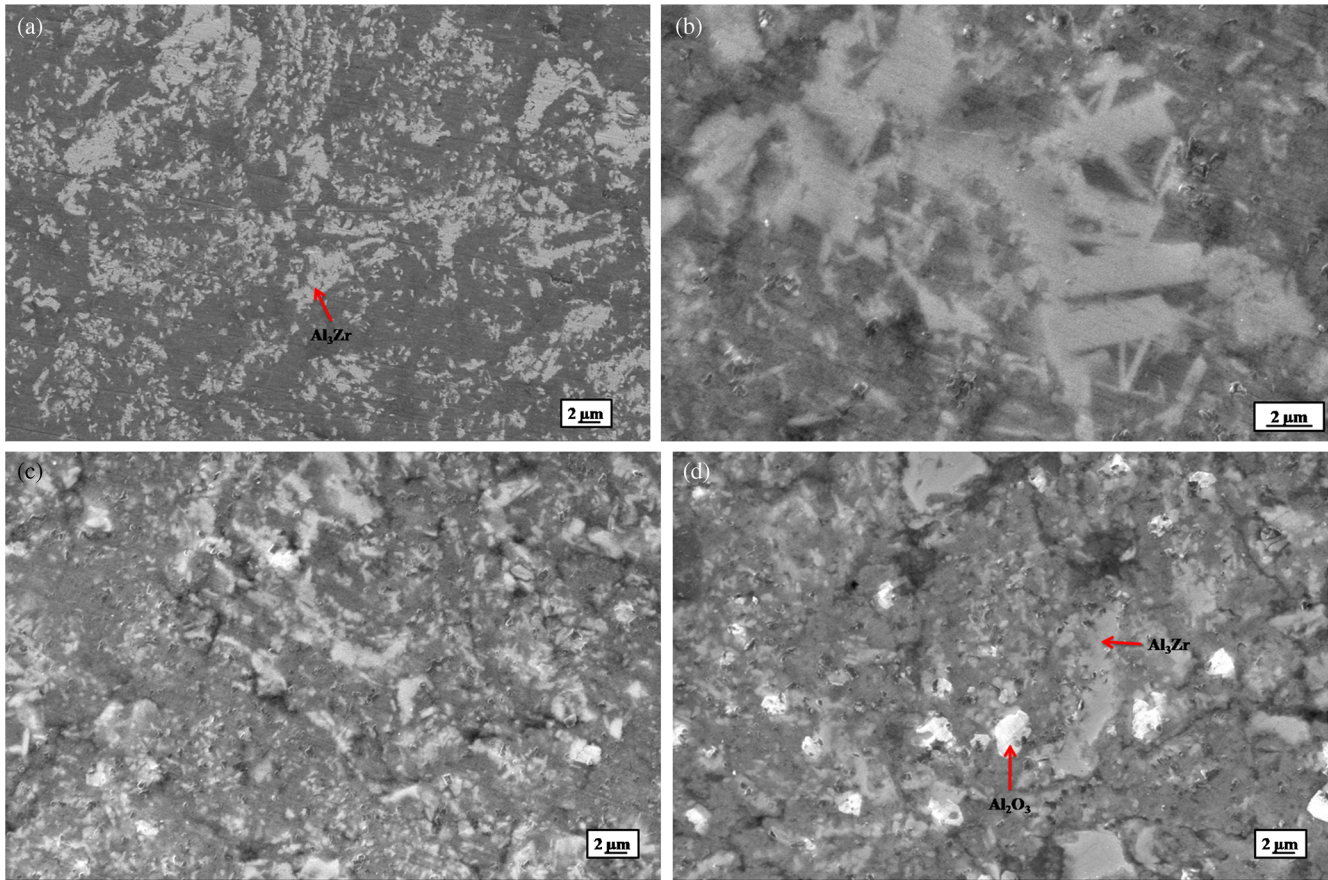


Figure 6. SEM micrographs of A20Z sample sintered at (a) 700, (b) 750, (c) 800 and (d) 850°C.

very small in size up to 750°C. Then these are grown in size at 800°C. Microstructures of compacts of A20Z composite sintered at 700, 750, 800 and 850°C are shown in figure 6a, b, c and d, respectively. The matrix is reinforced with high amount of Al_3Zr at 700°C in case of A20Z composite. The morphology of Al_3Zr phase is different and looks like chunky precipitates. Al_2O_3 particles are observed at 800°C. Al_2O_3 particles grow in size as the temperature increases.

XRD patterns of the sintered samples of A5Z, A10Z and A20Z composites are shown in figure 7a, b and c, respectively. It is clear that Al_3Zr particles are formed at 700°C. From the reaction ($3\text{ZrO}_2 + 13\text{Al} \rightarrow 3\text{Al}_3\text{Zr} + 2\text{Al}_2\text{O}_3$), it is clear that Al_2O_3 peaks should also be present in this diffraction pattern, but they are relatively weak compared to Al_3Zr peaks particularly in A5Z and A10Z samples. It is well known that the magnitude of the atomic scattering factor of Al_3Zr is far superior to the one corresponding to Al_2O_3 . This in turn accounts for the large intensity difference between Al_3Zr and Al_2O_3 peaks.

3.2b Hardness variation: Figure 8a, b, and c shows the variation of hardness with sintering temperature for A5Z and A10Z and A20Z, respectively. It is observed that for Al matrix composites (A5Z, A10Z and A20Z), the hardness decreases with the increase in sintering temperature. The maximum hardness of these composites is observed at

700°C. The reaction between Al and ZrO_2 ($13\text{Al} + 3\text{ZrO}_2 \rightarrow 3\text{Al}_3\text{Zr} + 2\text{Al}_2\text{O}_3$) completes at 700°C, and therefore, the hardness values are maximum at this temperature. With increasing sintering temperature, the grains of matrix as well as reinforcements grow in size and consequently, the hardness decreases. The variation of hardness as a function of ZrO_2 content for sintering temperatures of 700°C and 750°C is shown in figure 9a and b, respectively. Hardness increases with the increasing wt% of ZrO_2 in the composite for same sintering temperature. Both the ceramic (Al_2O_3) and intermetallic (Al_3Zr) reinforcements have much higher hardness than the matrix material. Therefore, the composite has a higher hardness than pure metal. Moreover, due to a large difference in the coefficient of thermal expansion value, a residual stress is developed inside the matrix. These two factors increase the hardness of the composite than pure metal.

3.3 Wear test results

3.3a Effect of reinforcements on sliding wear regimes: Figure 10a shows the volume loss vs. sliding distance plot for all the composites at 9.8 N normal loads. It is clear that volume loss is increasing with increasing sliding distance for all the composites. A5Z composite is seizing at this load, but A10Z composite can withstand this load. With an increase in wt% of ZrO_2 in the composite, the volume loss

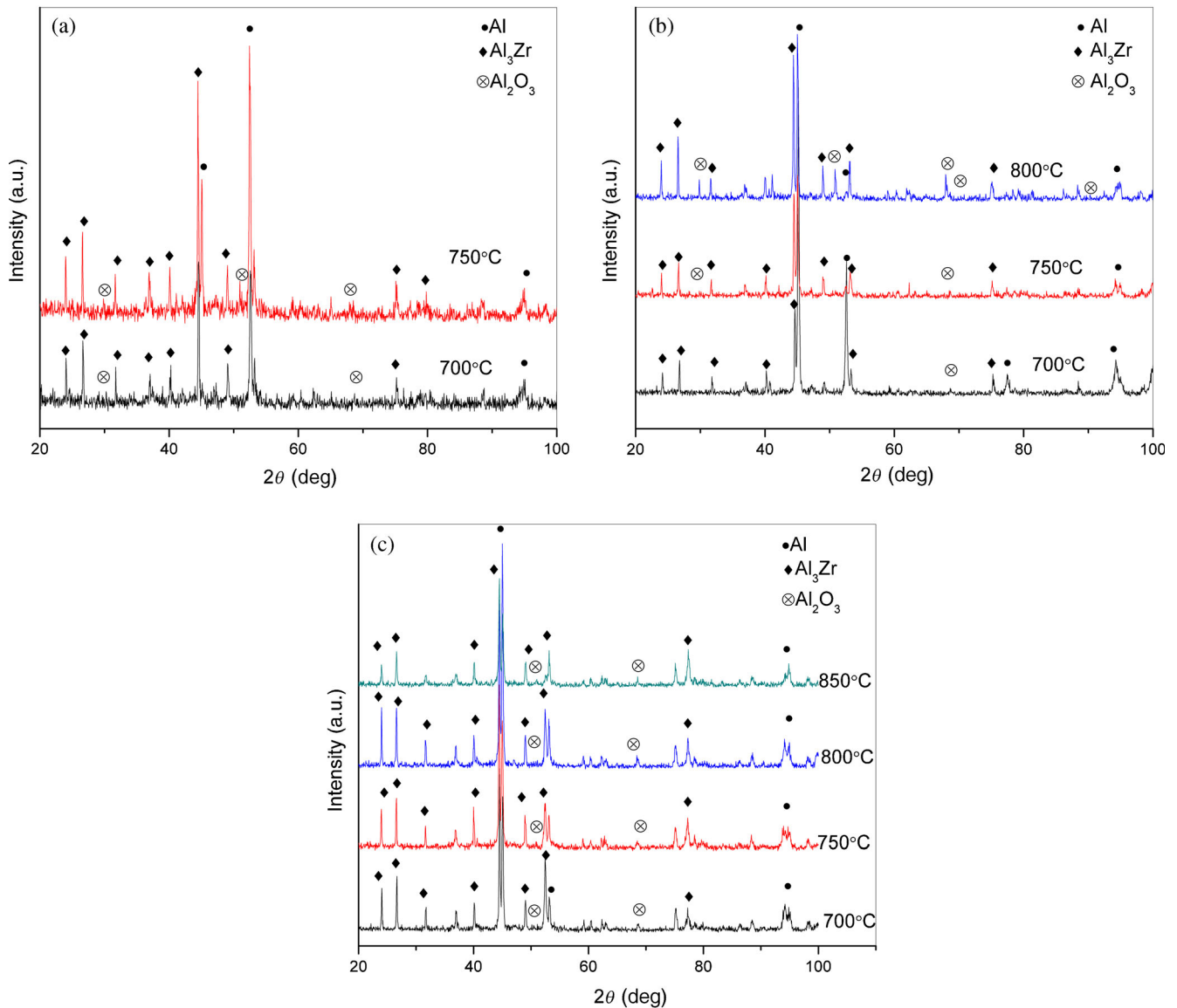


Figure 7. XRD pattern for (a) A5Z, (b) A10Z and (c) A20Z samples after sintering.

decreases. According to Archard's law [17], the volume loss is (a) inversely proportional to the hardness of the surface being worn away, (b) proportional to the sliding distance, and (c) directly proportional to the normal load. Therefore, the volume loss of the same load decreases due to increase in the hardness of the composite. Figure 10b shows the wear rate vs. sliding distance plot at 9.8 N normal loads for all the composites. Initially, the wear rate is very high because the oxide layer and the matrix are easily worn away by the SiC abrasive paper. With increasing sliding distance, the matrix becomes strain harden and the faces of reinforcements are open [16]. Both these factors resist wear of the composite. Therefore, the wear rate decreases and becomes steady after around 200 m of sliding distance.

3.3b Effect of normal load on sliding wear regimes: Figure 11a shows the change in volume loss with an increasing applied load for A10Z composite. It is noted that volume loss

increases with an increase in applied load. Figure 11b shows the variation of wear rate with increasing normal load for A10Z composite. The wear rate is much higher at higher load. This result matches with Archard's law to abrasive wear.

3.3c Variation of coefficient of friction: Variation of coefficient of friction with load for A10Z composite is shown in figure 12a. The coefficient of friction for every load is initially high and it is decreased to a steady state. The coefficient of friction has increased with increasing normal load from 4.9 to 7.35 N. This is due to less material removal from the worn surface at lower load. According to the theory of sliding friction, the friction force (F) is proportional to the normal load (L). The friction coefficient (μ) is defined as the ratio between friction force (F) and normal load (N). With increasing normal load (N), friction force (F) also increases and the ratio of these two forces known as friction coefficient (μ)

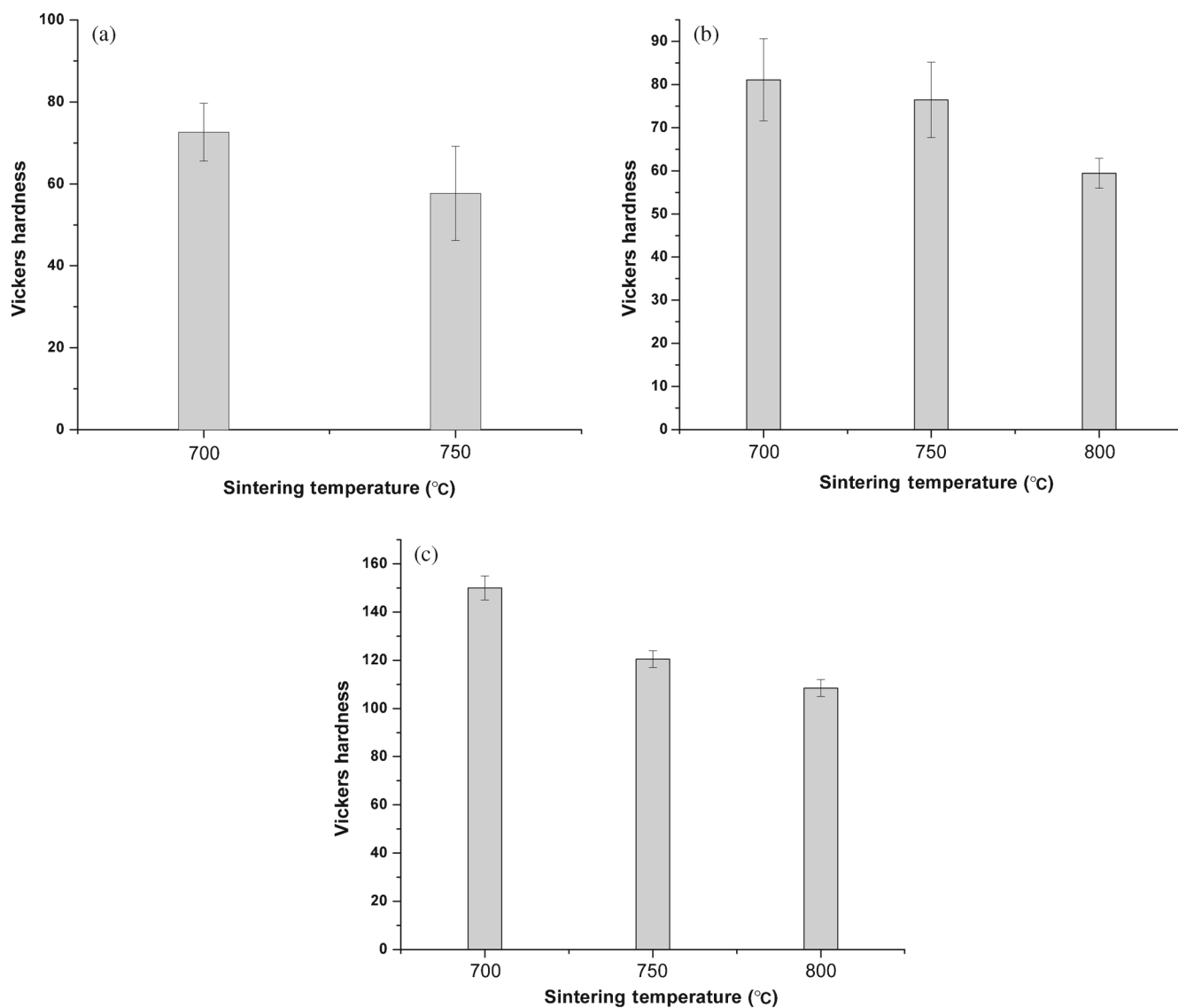


Figure 8. Variation of hardness with sintering temperature: (a) A5Z, (b) A10Z and (c) A20Z.

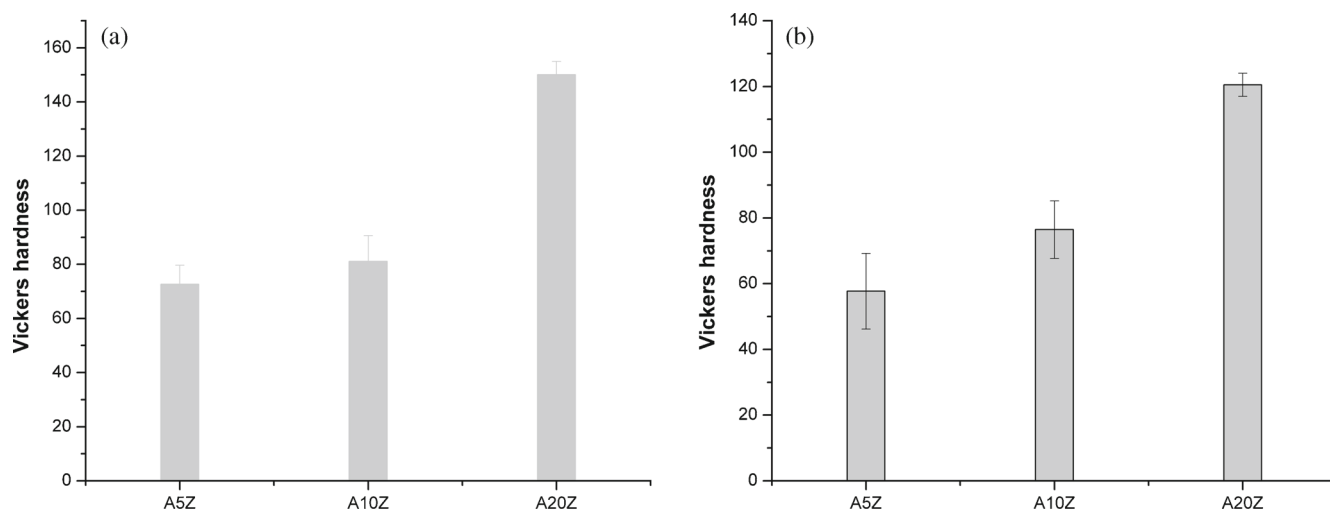


Figure 9. Variation of hardness as a function of ZrO₂ content: (a) 700 and (b) 750°C.

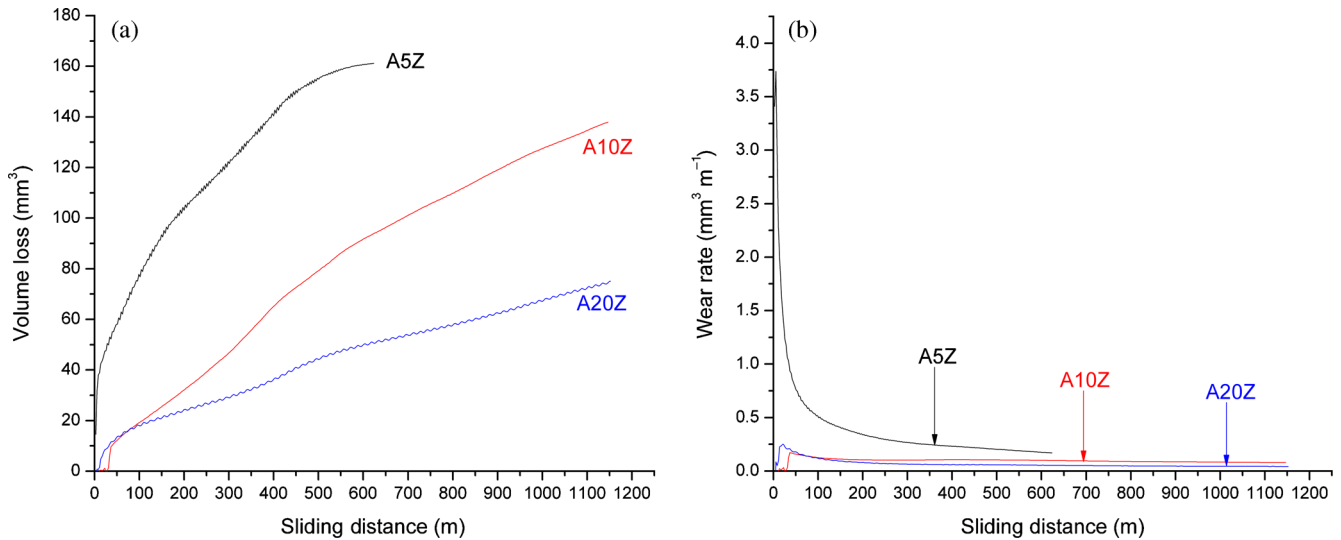


Figure 10. (a) Volume loss vs. sliding distance plot at 9.8 N load and (b) wear rate vs. sliding distance plot at 9.8 N load.

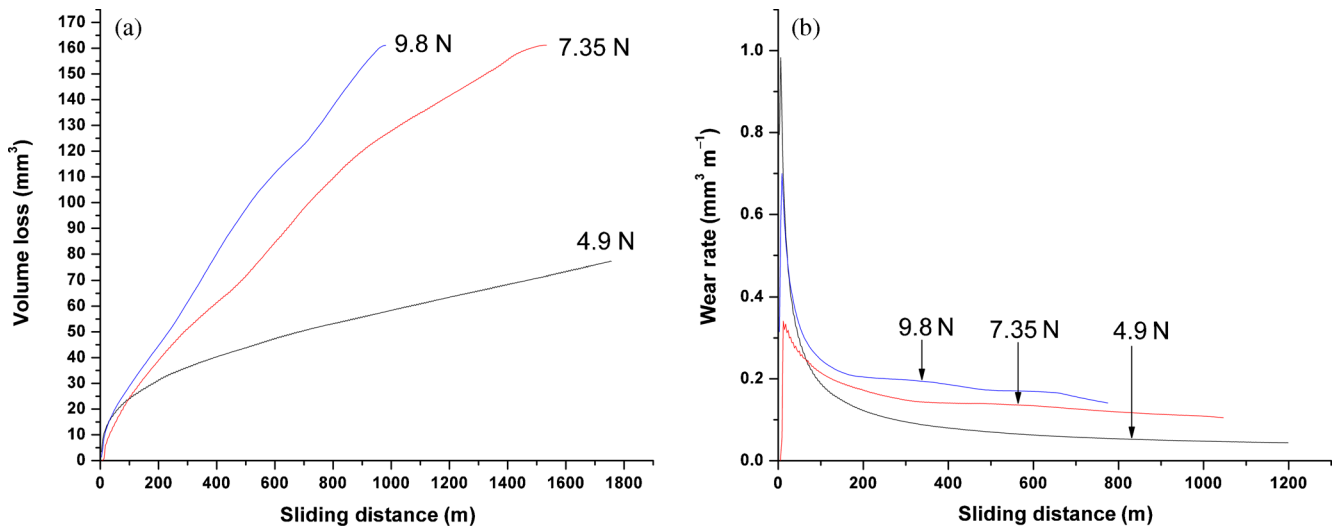


Figure 11. (a) Volume loss vs. sliding distance plot for A10Z at different loads and (b) wear rate vs. sliding distance for A10Z composite at various loads.

increases [17]. Therefore, the friction coefficient (μ) is highest at 7.35 N (maximum) load. Variation of the coefficient of friction at 9.8 N normal loads for A10Z and A20Z composite is shown in figure 12b. The coefficient of friction has decreased with the increase in ZrO₂ content. This is due to increase in hardness with the increase in ZrO₂ content. Therefore, the material removal decreases. As per the theory of abrasive wear, the amount of wear is inversely proportional to the hardness of the surfaces being worn away. With increasing hardness, the amount of wear decreases and therefore, the wear/friction coefficient also decreases in a similar way. Surface roughness also decreases with increasing ZrO₂ content. Abrasive wear arises when a hard rough surface slides against a softer surface, digs into it, and ploughs a series of grooves [21]. In the present case, 220-grade SiC grits act as hard surfaces and the cylindrical composite consisting

of Al–Al₃Zr–Al₂O₃ acts as soft surface. With increasing volume fraction of the reinforcements, the hardness of the composite increases and the amount of wear decreases. The mechanism of abrasive wear suggests that wear occurs by microcutting and microploughing mechanism [19]. Reinforcement in composite material acts as load bearer and hinders microploughing. Hence, surface roughness decreases with the increase in volume fraction of reinforcement. These parameters account for lower coefficient of friction for A20Z composite. A20Z composite has shown a minimum average coefficient of friction (0.35–0.5).

3.3d Morphology of wear surface: Figure 13a, b and c shows typical worn surfaces of A5Z, A10Z and A20Z composites, respectively, at 9.8 N loads. All the worn surfaces have grooves, damaged regions and plastic flow lines. The

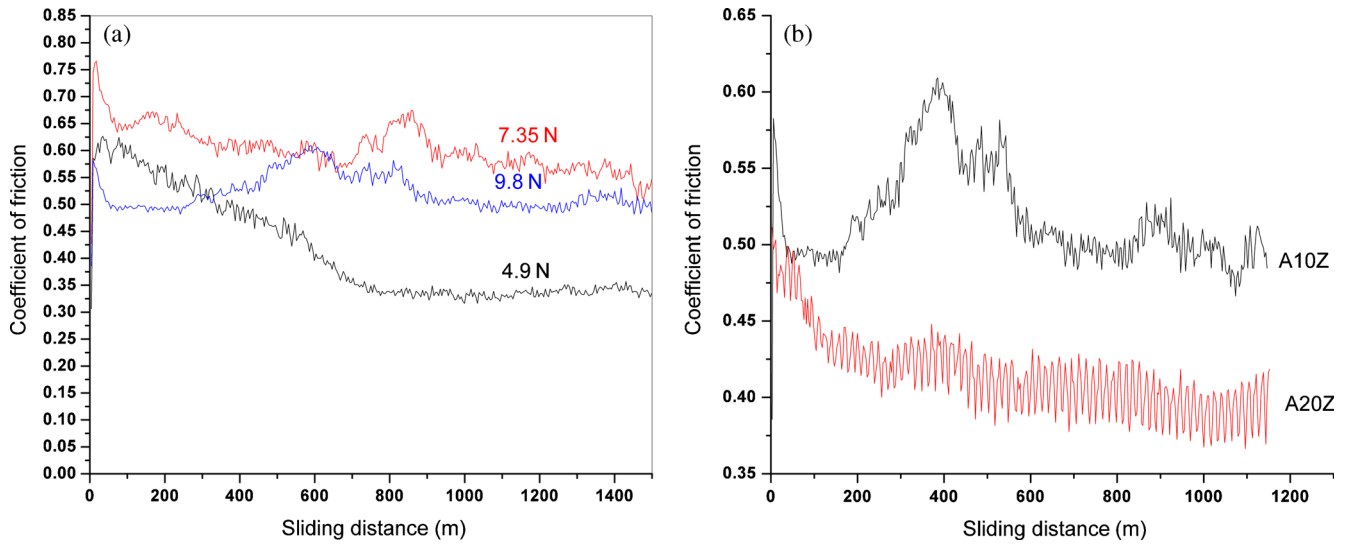


Figure 12. Variation of coefficient of friction with (a) load for A10Z composite and (b) with variation of coefficient of friction % ZrO₂ content.

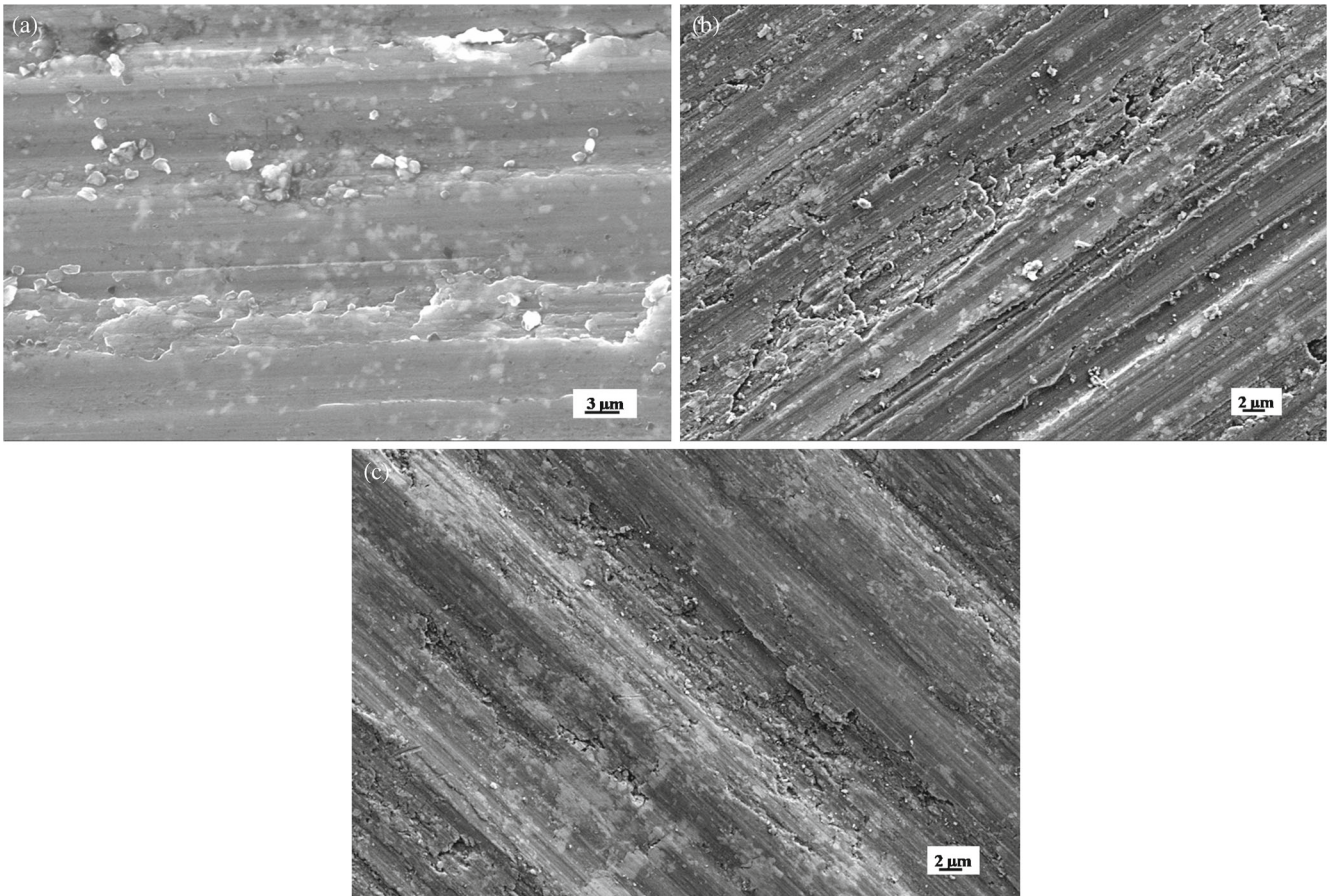


Figure 13. SEM micrographs of worn surface at 9.8 N load: (a) A5Z, (b) A10Z and (c) A20Z.

width and depth of the grooves decrease with increasing % of ZrO₂ in the composite. The width and depth of the grooves generally imply the amount of material removed from the specimen surface. These two parameters depend primarily on the

effective load and the hardness of the composite surface. In view of this fact, it is expected that uniform distribution of the particle and small inter-particle distance will lead to a high wear resistance. By the increase in ZrO₂%, the

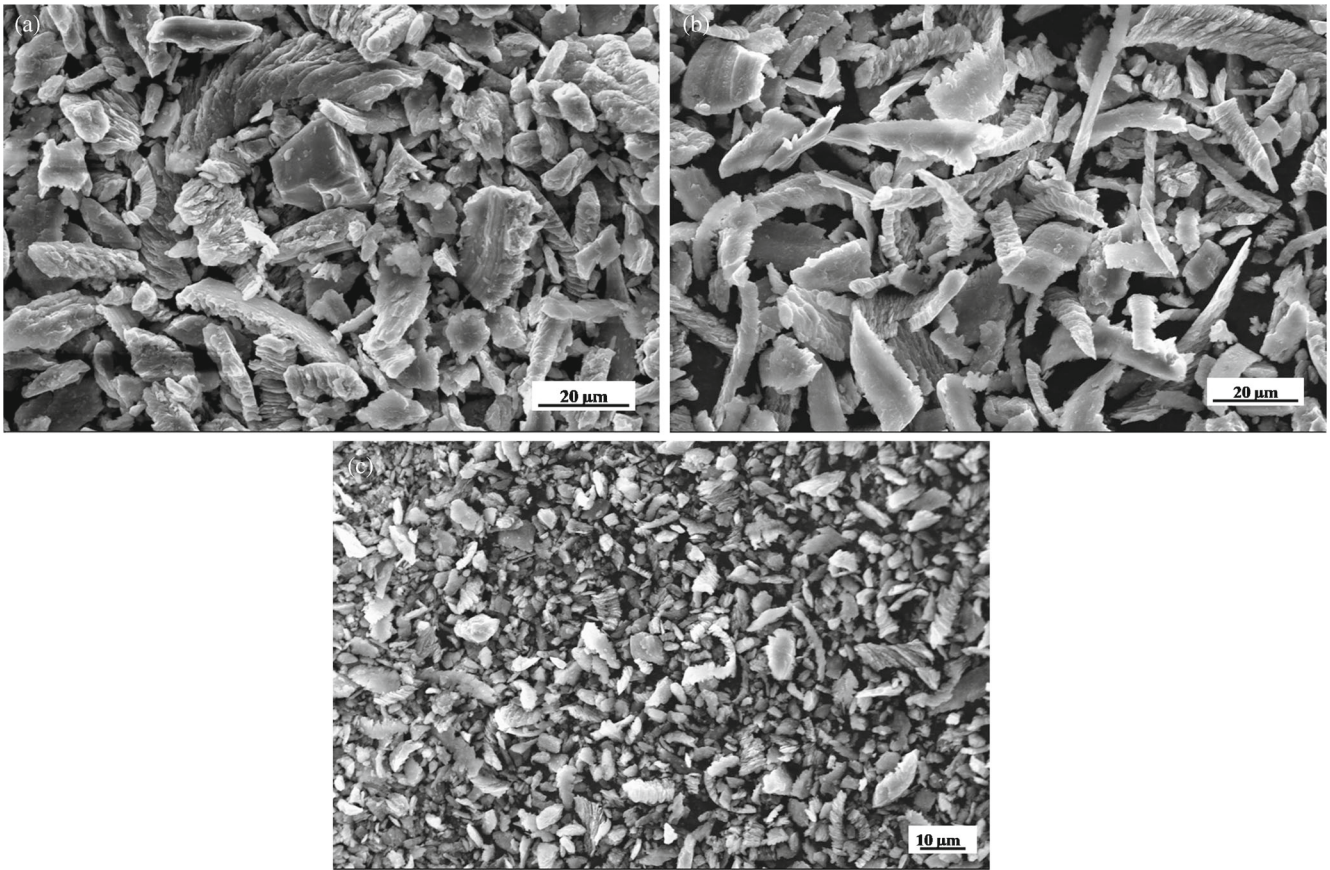


Figure 14. SEM micrographs of wear debris: (a) A5Z, (b) A10Z and (c) A20Z.

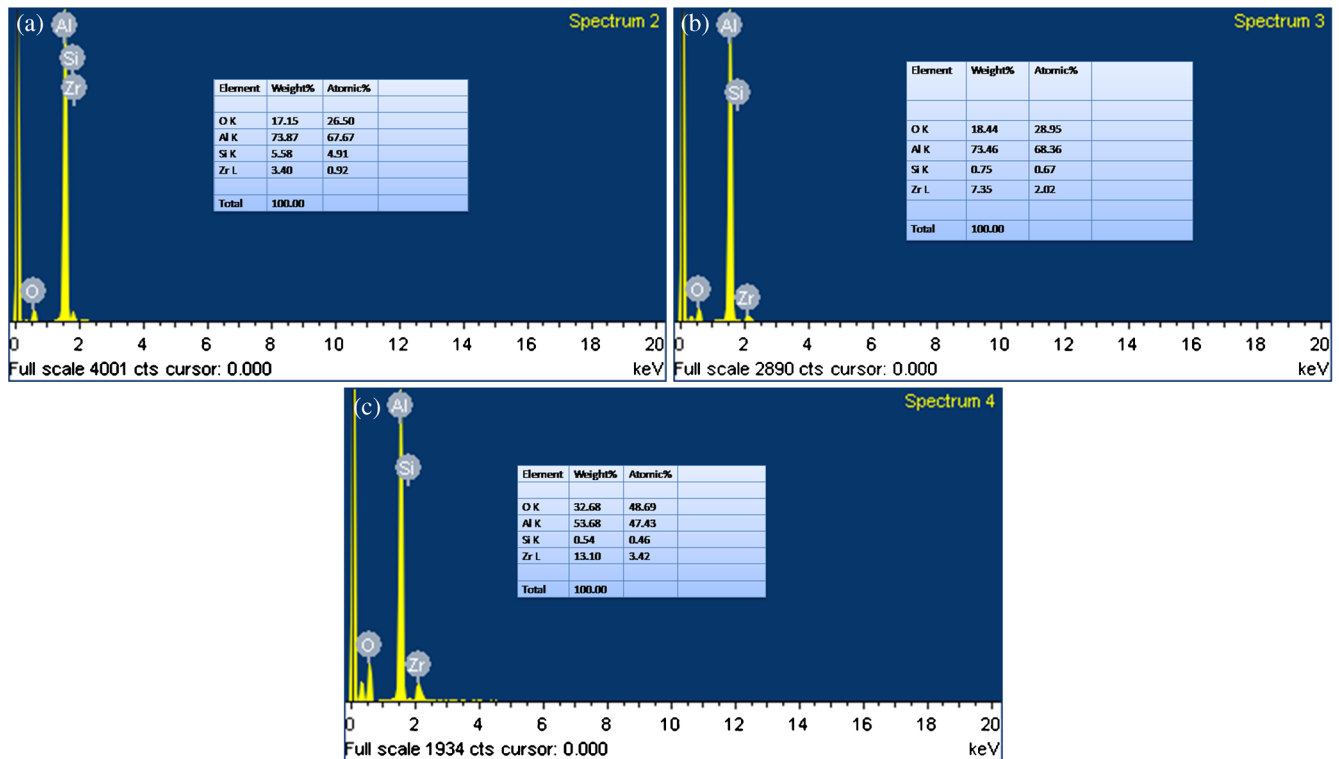


Figure 15. EDS spectrum from wear debris: (a) A5Z, (b) A10Z and (c) A20Z.

worn surface of the composite has relatively smooth surface. Figure 13b shows typical worn surfaces of A10Z composites after 1200 m sliding distance at 9.8 N load. The wear surface shows continuous groove formation [18], damaged regions, crack propagation and fracturing. The grooves generate due to microploughing [19] of the surface. Extensive surface ploughing [9] with the local delamination is observed at higher load. Irregular plastic flow lines can be seen indicating the occurrence of extensive plastic deformation during the wear.

3.3e Characterization of wear debris: The worn debris of metal matrix composites of A5Z, A10Z and A20Z is shown in figure 14a, b and c, respectively. A substantial quantity of wear debris is generated during the test. Debris particles have three morphologies: ribbon type, plate type and welded matrix of the massive particles. As suggested by some researchers, ribbon-type debris are characteristics of cutting and ploughing action of hard abrasive particles, plate types are characteristics of adhesion between metal-metal and welding of the matrix may occur because of the continuous rubbing action of samples on wear track [20,21]. All the particles are irregular in shape, size and distribution. Actually, all these wear debris particles are present in all the tests, the only difference is the relative amount of each type, and this could be influenced to a great degree by normal load and sliding velocity. The sizes of the particles or plates are larger for higher loads. The volume of the wear debris increases with increasing normal loads and sliding velocity, thereby resulting in greater wear loss for higher loads and sliding velocities. The EDS analysis in figure 15 shows the presence of Al, Zr, Si and O. The analysis clearly shows that the weight fraction of Zr in the debris is increasing from 3.4% for A5Z to 7.35% for A10Z and 13.10% for A20Z, respectively. It indicates that Zr plays an important role to resist wear in Al-ZrO₂-based composite.

4. Conclusions

Al₃Zr- and Al₂O₃-reinforced Al matrix composites were successfully synthesized using mechanical and thermal treatments. No reaction occurred in the Al-ZrO₂ system during ball-milling up to 15 h. The exothermic reaction temperature between Al and ZrO₂ drastically reduced owing to high-energy ball-milling. The Al matrix composites (5, 10 and 20 wt% ZrO₂) showed maximum hardness at

a sintering temperature of 700°C. The hardness of the composite increased with the increase in amount of ZrO₂ and decreased with the increase in sintering temperature above 700°C. The wear resistance increased with the increase in amount of ZrO₂ in the composite. Microcutting and microploughing were the predominant mechanisms of wear. The coefficient of friction decreased with the increase in amount of ZrO₂ in the composite and with the decrease in normal load.

References

- [1] Reddy B S B, Das K and Das S 2007 *J. Mater. Sci.* **42** 9366
- [2] Li Y, Ramesh K T and Chin E S C 2000 *Int. J. Solids Struct.* **37** 7547
- [3] Tjong S C and Ma Z Y 1997 *Compos. Sci. Technol.* **51** 697
- [4] Massardier V, Fougères R and Marle P 1995 *Mater. Sci. Eng. A* **203** 93
- [5] Shyu R F and Ho C T 2006 *J. Mater. Process. Technol.* **171** 411
- [6] Zhiqiang S, Di Z and Guobin L 2005 *Mater. Des.* **26** 454
- [7] Urena A, Rams J, Escalera M D and Sanchez M 2005 *Compos. Sci. Technol.* **65** 2025
- [8] Biswas S K and Pramila Bai B N 1981 *Wear* **68** 347
- [9] Sudarshan and Surappa M K 2008 *Wear* **265** 349
- [10] Wang S, Guo P, Yang L, Zhao F and Wang Y 2009 *Mater. Des.* **30** 704
- [11] Zhao Y T, Zhang S L, Chen G, Cheng X N and Wang C Q 2008 *Compos. Sci. Technol.* **68** 1463
- [12] Abdizadeh H and Baghchesara M A 2013 *Ceram. Int.* **39** 2045
- [13] Suryanarayana C 2001 *Progr. Mater. Sci.* **46** 21
- [14] Li G R, Zhao Y T, Wang H M, Chen G, Dai Q X and Cheng X N 2009 *J. Alloys Compd.* **471** 530
- [15] Zeng Z M 2003 *Manual of mechanical engineering materials* (Peking: Mechanical Industry Publishing Company)
- [16] Yilmaz Y and Buytoz S 2001 *Compos. Sci. Technol.* **61** 2381
- [17] Rabinowicz E 1995 *Friction and wear of materials*, 2nd edn (The University of Michigan: Wiley, New York)
- [18] Miyajima T and Iwai Y 2003 *Wear* **255** 606
- [19] Srivastava A K and Das K 2008 *Mater. Lett.* **62** 3947
- [20] Ramesh C S, Anwar Khan A R, Ravikumar N and Savanprabhu P 2005 *Wear* **259** 602
- [21] Durai T G, Das K and Das S 2007 *Mater. Sci. Eng. A* **471** 88